Characterization of NiCo2O4 electrodes for O2 evolution. Part II. Non-electrochemical characterization of NiCo2O4 electrodes

J. Electroanal. Chem., 208 (1986) 297–321
Elsevier Sequoia S.A., Lausanne – Printed in The Netherlands

CHARACTERIZATION OF $NiCo_2O_4$ ELECTRODES FOR O_2 EVOLUTION

PART II. NON-ELECTROCHEMICAL CHARACTERIZATION OF $NiCo_2O_4$ ELECTRODES

J. HAENEN *, W. VISSCHER and E. BARENDRECHT

Laboratory for Electrochemistry, Department of Chemical Technology, Eindhoven University of Technology, P.O. Box 513, 5600 MB Eindhoven (The Netherlands)

(Received 18th October 1985; accepted 24th March 1986)

ABSTRACT

$NiCo_2O_4$ spinel oxide was characterized by a number of ex situ non-electrochemical techniques. Thermogravimetric analysis was applied to study the course of the decomposition of the metal nitrates in order to determine the temperature range of the spinel oxide phase. The surface morphology of $NiCo_2O_4$ was investigated using BET measurements and scanning electron microscopy. X-Ray diffraction, temperature-programmed reduction (TPR) and X-ray and Auger photoelectron spectroscopy (XPS and Auger) were employed to study the surface and bulk composition of $NiCo_2O_4$. On the basis of the TPR data, $NiCo_2O_4$ can be presented as $M^{2+}M_2^{3+}O_4$, with an average oxidation state of the metal cation M (M = Ni or Co) equal to 2.67+. The presence of divalent nickel is proposed on the basis of the binding energy of the Ni2$p_{3/2}$ photoelectron line, and of cobalt as mainly diamagnetic Co^{3+} in a low-spin state, and paramagnetic divalent high-spin cobalt based on the satellite structure in the XPS spectrum.

(I) INTRODUCTION

The influence of the preparation technique and conditions on the anodic performance of $NiCo_2O_4$ spinel oxide as an electrocatalyst for anodic oxygen evolution has been investigated in ref. 1. In Part I [2], the electrochemical characterization of the $NiCo_2O_4$ surface features has been given. In this part, a number of ex situ non-electrochemical techniques are used to characterize the nickel–cobalt spinel system in order to provide supplementary information about the surface features of $NiCo_2O_4$, in particular with reference to heat treatment.

Thermogravimetric analysis was applied to study the course of the decomposition of cobalt nitrate as a function of the temperature. BET measurements and scanning

* Present address: DSM Central Laboratory, Department of Catalysis, P.O. Box 18, 6160 MB Geleen, The Netherlands.

0022-0728/86/$03.50

electron microscopy were used for the investigation of the surface morphology. X-Ray diffraction, temperature-programmed reduction and X-ray and Auger photoelectron spectroscopy were employed to study the surface and bulk composition of $NiCo_2O_4$.

(II) THERMOGRAVIMETRIC ANALYSIS

Thermogravimetric analysis (TGA) was carried out using a Mettler thermoanalyzer 2. The heating rate was 3°C min^{-1} in the temperature range of 25–1000°C.

Figure 1 shows the thermogravimetric diagram of the decomposition of $Co(NO_3)_2 \cdot 6\ H_2O$ (Merck), and of $Ni(NO_3)_2 \cdot 6\ H_2O$ (Merck) and $Co(NO_3)_2 \cdot 6\ H_2O$ mixed in a stoichiometric ratio of 1:2. The TGA curves are plotted as a fraction of the initial weight $(G_0 - G)/G_0$ vs. the temperature (G_0 is the initial weight and G is the weight loss of the sample). It appears that in both cases decomposition occurs below 300°C. It is well known that both decomposition processes give rise to the formation of a spinel oxide, i.e. in the former, Co_3O_4, and in the latter, $NiCo_2O_4$. The TGA curve of cobalt nitrate can be separated into different regions: a major weight loss region below 280°C which can be divided into two parts, followed by a very small monotonic weight loss up to 500°C. Then no further weight loss takes place in the temperature range of 500–900°C. Finally, a sharp weight loss is observed at 900°C.

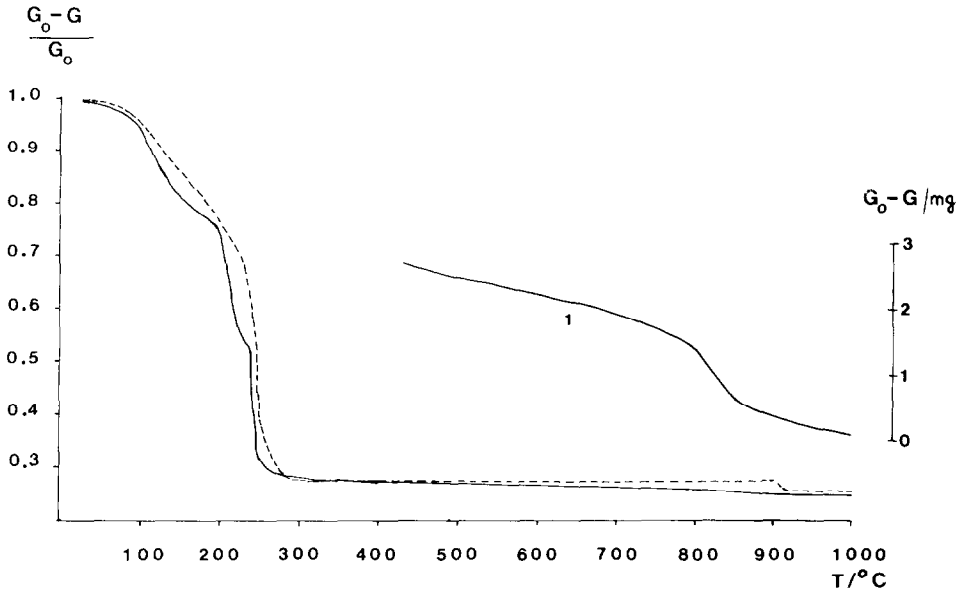

Fig. 1. Thermogravimetric curves plotted as a fraction of the initial weight vs. temperature. (– – –) $Co(NO_3)_2\ 6\ H_2O$; (———) $Ni(NO_3)_2 \cdot 6\ H_2O \cdot Co(NO_3)_2 \cdot 6\ H_2O = 1\ 2$; (1) part of the solid curve on an expanded real weight scale.

The hydration water molecules are removed in the temperature range below 230°C, as confirmed by calculations of the weight-loss curve. The decomposition of the nitrate, with the evolution of NO_x, apparently starts as soon as the dehydration is completed. It takes place over a short temperature interval of about 50°C and results in the spinel oxide Co_3O_4. The weight at 280°C does not correspond exactly to that of Co_3O_4. The presence of hydration water in excess over the nominal composition can disturb the calculations based on the TGA curve. $Co(NO_3)_2 \cdot 6 H_2O$ is known to be extremely deliquescent [3]. The temperature at which the spinel oxide is formed changes with the heating rate. Pope et al. [4] observed that the decomposition was already completed at 200°C when the heating rate was lowered, while Garavaglia et al. [5] reported that at sufficiently long times Co_3O_4 is even formed at 150°C (24 h). The small monotonic weight loss observed in the temperature range of 280–500°C has been related to the progressive loss of excess oxygen in the initially non-stoichiometric oxide [5–8]. Further heating of the sample does not result in any change in weight up to 900°C. This indicates that the spinel-type oxide does not undergo further conversion in this temperature range. At about 900°C, a sharp decrease in the curve is noticed: the spinel oxide Co_3O_4 decomposes to CoO, as indicated by the weight loss.

The TGA curve of the mixed nitrates is initially similar to that obtained for the cobalt nitrate: a sharp weight loss takes place immediately on heating, tapering off above 275°C, at which the processes mentioned earlier take place, i.e. fusion of the salt, dehydration and decomposition of the mixed nitrates. Thereafter, a steady weight loss starting at 275°C up to 800°C is observed, followed by a more pronounced weight loss above 800°C (as shown by curve 1 on an expanded weight scale in Fig. 1).

It can be suggested that $NiCo_2O_4$ is already formed after the nitrate decomposition is finished (at about 275°C). Further increase in the temperature up to about 400°C causes a weight loss, which can be correlated with the loss of excess oxygen of $NiCo_2O_{4+x}$. The weight loss above 400°C can then be interpreted as the thermal decomposition of the spinel oxide $NiCo_2O_4$. The sharp decrease above 800°C has been attributed to the loss of all spinel phases [9].

From the weight loss in the range 300–400°C the excess oxygen, i.e. the value of x in $NiCo_2O_{4+x}$, can be calculated from the thermogram using the equation

$$x = \frac{(G_T - G_S)}{G_S} \times \frac{240.56}{16} \tag{1}$$

where G_T is the weight of the sample at temperature T, G_S is the weight expected for the stoichiometric compound formed and the constants in the numerator and denominator are the molecular mass of $NiCo_2O_4$ and the atomic mass of oxygen, respectively. The results are shown in Table 1. It appears that the stoichiometric composition is reached at about 360°C. At 400°C, a negative value of x is found, which indicates the decomposition of the spinel structure. This number has no physical meaning above 400°C, i.e. in the two-phase region.

However, the restrictions of the calculation based on a simple weight-loss curve

TABLE 1

Oxygen content in $NiCo_2O_{4+x}$ obtained from thermal analysis of the mixed nickel–cobalt nitrate

$T/°C$	300	350	400
x	+0.40	+0.03	−0.14

must be borne in mind. The values were derived from TGA, which gives non-equilibrium data. It was also found that when the TGA curve is interrupted and held constant, the weight loss still changes considerably. The calcination time is important here, especially at lower temperatures ($\leq 300°C$). Further, the presence of excess hydration water can disturb the calculation. The thermogravimetric analysis of the cobalt nitrate and the mixed cobalt nitrate is in agreement with the results obtained by other authors [3–12].

(III) BET SURFACE AREA

Surface areas were measured using the BET method. The pore size distribution was also determined. The $NiCo_2O_4$ powder samples were prepared by thermal decomposition as described earlier [1].

Figure 2 illustrates the effect of the temperature T_F and duration time t_F of the heat treatment on the BET surface area of the $NiCo_2O_4$ powders. The specific surface areas decrease with increase of T_F and with t_F. At each temperature T_F, the surface area of $NiCo_2O_4$ reaches a constant value as the duration time t_F is increased. So, at each temperature T_F, a duration time t_F exists beyond which no

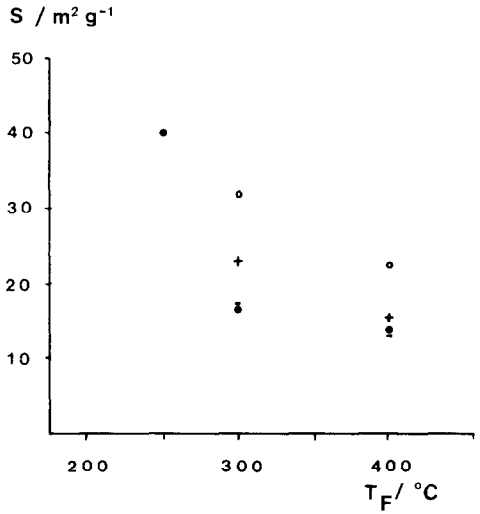

Fig. 2. BET surface area of $NiCo_2O_4$ powders as a function of the temperature T_F. (○) $t_F = 1$ h; (+) $t_F = 5$ h; (●) $t_F = 10$ h; (−) $t_F = 24$ h

TABLE 2

BET surface areas of $NiCo_2O_4$ powders and apparent electrochemical surface areas of $NiCo_2O_4$ electrodes as a function of T_F and t_F

Heat treatment		BET surface area of $NiCo_2O_4$ powders /$m^2\ g^{-1}$	Apparent electrochemical surface area of $NiCo_2O_4$ electrodes/$m^2\ g^{-1}$ [2]
T_F/°C	t_F/h		
250	10	39.9	10.7
300	1	32.0	6.9
300	10	16.0	5.9
350	1	—	4.5
400	1	22.5	3.1
400	10	13.7	2.5
			3 3

significant changes in surface area are observed; this value is, of course, reached faster at higher T_F. The difference in surface area in this limit, i.e. $t_F = 24$ h, between the heat treatment of 300 and 400°C is 25%. This differs from the cyclic voltammetric results [2], where the charge was proposed to be a measure of the surface area of the $NiCo_2O_4$ electrode. The voltammetric charge depends strongly on T_F, but only slightly on t_F. Virtually no further change in surface area after a heat treatment of 1 h was observed. It was found that the difference in surface area between the heat treatment at 300 and 400°C was about 100%.

The BET surface areas of the $NiCo_2O_4$ powder materials and the apparent electrochemical surface areas of the $NiCo_2O_4$ electrodes [2] are compared in Table 2. They show the same dependence with respect to temperature T_F: a decrease of the surface area with increasing T_F.

The dependence of the surface area on the duration time t_F shows that when a voltammetric technique is used, an approximately constant surface area is reached faster. Apparently, no further sintering takes place after a heat treatment of 1 h, while in the case of powder material at least a thermal treatment of 10 h at 300°C or 5 h at 400°C is required. The discrepancies in the magnitude of the surface area as a function of T_F and t_F between the powder and electrodes can be explained by a difference in the morphology of the $NiCo_2O_4$ oxide due to the slightly different preparation conditions. Unfortunately, it was not possible to subject the $NiCo_2O_4$ electrodes as such to a BET examination.

A pore size distribution was carried out on $NiCo_2O_4$ powder samples, prepared (a) at a temperature T_F of 300°C and for a duration time of 1 h, (b) at 400°C for 1 h and (c) at 400°C for 24 h. In describing pore size, the notation of Dubinin [13] is commonly adopted: micropores are pores with a diameter of less than 2 nm, mesopores have diameters in the range of 2–30 nm and macropores are those larger than 30 nm. The samples showed no distinct mean pore diameter; they were spread in the mesopore range. It appeared that there were no micropores. In sample (a) most pore diameters are situated in the range 2–5 nm, in sample (b) 5–15 nm, and in sample (c) from 7 to 20 nm.

TABLE 3

Values of the interplanar d-spacing (in Å = 0.1 nm), the Miller indices and the relative intensities of the $NiCo_2O_4$ electrodes as a function of T_F and t_F

T_F/°C	t_F/h	*hkl*																					
		111		220		311		⟨111⟩		222		⟨200⟩		400		422		511,333		⟨220⟩		440	
		d	I/I_1	d	I/I_1	d	I/I_1	d	I/I_1	d	I/I_1	d	I/I_1	d	I/I_1	d	I/I_1	d	I/I_1	d	I/I_1	d	I/I_1
250	10	4.68	24	2.88	32	2.45	100			2.34	24			2.03	85	1.66	14	1.56	35			1.43	38
300	1	4.70	19	2.87	32	2.45	100			2.34	22			2.03	68	1.65	16	1.56	36			1.43	50
300	10	4.66	15	2.87	33	2.45	100			2.35	19			2.03	54	1.66	16	1.56	32			1.43	48
350	1	4.66	19	2.86	30	2.45	100			2.34	27			2.03	60	1.65	19	1.56	40			1.43	54
400	1	4.68	15	2.87	28	2.45	100			2.35	14			2.03	41	1.66	14	1.56	33			1.43	44
400	10	4.69	13	2.87	32	2.45	100			2.35	20			2.03	48	1.66	15	1.56	35			1.43	44
500	1	4.68	14	2.87	31	2.45	100	2.41	10	2.35	14	2.09	10	2.02	55	1.66	10	1.56	34	1.48	9	1.43	47
600	1	4.66	12	2.86	36	2.44	100	2.41	33	2.34	12	2.09	40	2.03	45	1.65	11	1.56	22	1.48	24	1.43	40
									(83)				(100)								(60)		
$NiCo_2O_4$	ASTM																						
	20.781	4.69	14	2.87	25	2.45	100			2.34	10			2.03	25	1.66	8	1.56	30			1.43	45
NiO	ASTM																						
	4-0835							2.41	91			2.09	100							1.48	57		

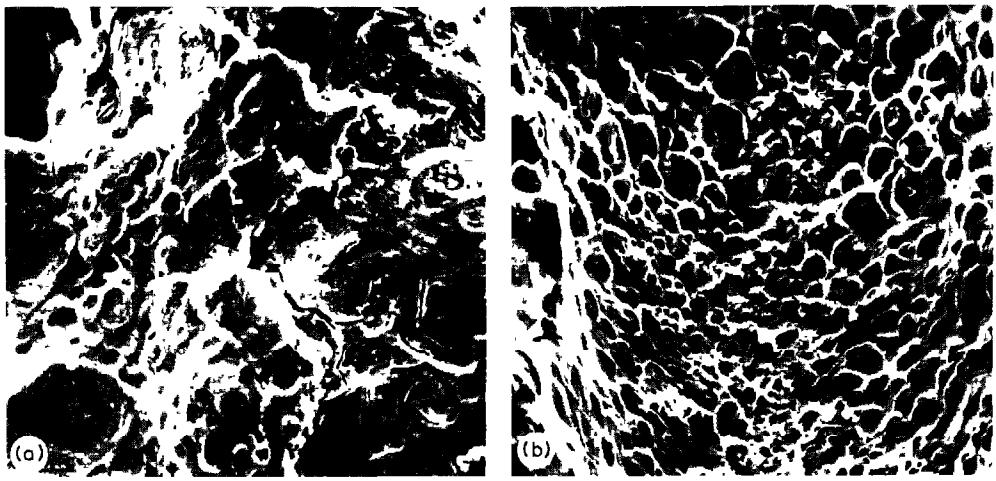

Fig 3. SEM micrographs of the surfaces of $NiCo_2O_4$ electrodes prepared at different temperatures T_F. (a) 300 °C for 1 h; (b) 400 °C for 1 h. Magnification factor = 120.

Observation of the samples using scanning electron microscopy (SEM) gives additional evidence that the surface morphology is determined by the preparation temperature T_F. SEM micrographs of $NiCo_2O_4$ electrodes are shown in Fig. 3. The $NiCo_2O_4$ electrode prepared at 400 °C exhibits a smooth, circular scaly surface, while the electrode prepared at 300 °C shows a rougher and more porous texture. All coatings exhibit some cracks.

(IV) X-RAY DIFFRACTION

X-Ray diffraction analysis of the $NiCo_2O_4$ catalyst was carried out using a Philips model PW 1009 Röntgen diffraction spectrometer. FeKα radiation with a Mn filter was used. All diffraction patterns were recorded at room temperature. X-Ray diffraction patterns of the $NiCo_2O_4$ electrodes were also obtained using the Philips diffractometer.

The phase composition was identified by comparison with ASTM data [14].

There was little difficulty in identifying the phase present in the Debye–Scherrer powder photographs of freshly prepared $NiCo_2O_4$ as a function of T_F and t_F. With lower T_F and t_F, the diffraction lines became broader and less well defined. X-Ray analysis confirmed the expectations, i.e. the detection of the single-phase $NiCo_2O_4$ spinel oxide in the T_F range of 250–400 °C. The visually estimated intensities of the Debye–Scherrer diffraction lines were in agreement with the ASTM data of $NiCo_2O_4$ [14]. At higher temperatures, lines corresponding to another cubic phase were observed, presumably NiO. $NiCo_2O_4$ electrodes at which oxygen had been evolved were analysed by the spectrometric diffraction method.

Table 3 presents the values of the interplanar d-spacings, the Miller indices (hkl) and the relative intensity (referred to the strongest line I_1, i.e. $2\theta = 46.6°$) of the

$NiCo_2O_4$ coatings as a function of T_F and t_F, together with the ASTM data of $NiCo_2O_4$ and NiO. The X-ray diffraction patterns in the T_F range below 400°C are characteristic of the $NiCo_2O_4$ spinel. The deviation in the measured relative intensity, which seems to increase with decreasing temperature T_F, can be attributed to preferred orientations.

The appearance of NiO at T_F greater than 400°C is confirmed by the detection of the additional reflections at 2θ equal to 49.0° ($d = 2.41$), 55.2° ($d = 2.09$) and 81.8° ($d = 1.48$). The values in parentheses in Table 3 are the relative intensity I/I_1 referred to the strongest line I_1 of the additional lines, i.e. $2\theta = 55.2°$. The X-ray data analysis is in agreement with the TGA diagram (Section II), and furthermore reveals that the decomposition of the $NiCo_2O_4$ spinel sets in at temperatures above 400°C, with the appearance of NiO. With Röntgen diffraction, no influence of the oxygen evolution reaction on the $NiCo_2O_4$ electrodes was detected.

The parameter of the lattice when it corresponds to the closest packing principle is equal to 0.8 nm [15]. The cell parameter of spinels is usually greater than that predicted by the packing density principle. The reported unit cell dimensions of $NiCo_2O_4$ can be in the range of 0.810–0.812 nm [9,10,16,17]. The lattice parameter or unit cell dimension a_0 was simply determined from the observed d-spacings for the planes (311) and (440) by making use of the cubic formula for the interplanar spacing d,

$$a_0 = d\sqrt{h^2 + k^2 + l^2} \tag{2}$$

where h, k and l represent the Miller indices.

The unit cell dimensions determined from the Debye–Scherrer powder samples show a tendency to increase slightly (0.808–0.810 nm) in the T_F range of 250–400°C. Above 400°C, a decrease in a_0 was noticed. No appreciable variation in the lattice constant as a function of t_F was observed.

The lattice parameter of the coatings showed somewhat higher values, i.e. 0.810–0.812 nm, and more discrepancies in the temperature range below 400°C. The decrease in a_0 above 400°C was observed more clearly.

The observation of a decrease in a_0 values above 400°C in both cases, i.e. powder and coatings, might be related to the spinel decomposition. The difference in a_0 values in the T_F range of the spinel-only phase is suggested to be a result of the difference in measuring technique.

(V) TEMPERATURE-PROGRAMMED REDUCTION

(V.1) Experimental

Temperature-programmed reduction (TPR) was applied to investigate the reduction behaviour of the oxide catalyst $NiCo_2O_4$. In this technique, hydrogen is passed continuously over the catalyst, while the temperature is raised linearly with time. By measuring the consumption of hydrogen, due to the reduction of species in the

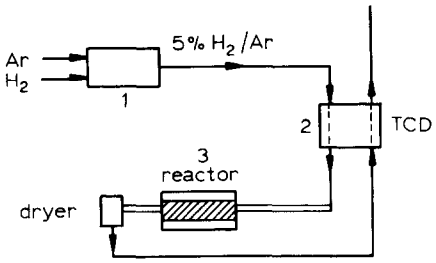

Fig. 4. Schematic drawing of the TPR apparatus. (1) Pneumatic gas dosage system for preparing 5% H_2 in Ar; (2) thermal conductivity cell; (3) reactor section: quartz tube placed in a silver block oven.

catalyst, as a function of the applied temperature, a so-called reduction profile is obtained. The total hydrogen consumption during the reduction enables the stoichiometric composition of the oxide to be determined. The ratio H_2/M is a measure of the total hydrogen consumption, and expresses the average number of dihydrogen molecules required for the reduction of a metal ion (M) in the oxide. So, TPR allows the determination of the mean valency state of the metal ions in the oxide and, therefore, is of great value in the characterization of the catalyst.

The TPR apparatus has recently been described in detail by Boer et al. [18]; a schematic drawing is presented in Fig. 4. The hydrogen consumption was measured by a thermal conductivity detector (TCD) of the diffusion type. The TCD is very sensitive in detecting small changes in the concentration of H_2 in Ar because of the differences in thermal conductivity between the active phase, H_2, and the inert phase, Ar. The heating rate during all TPR experiments was 5°C min^{-1}.

TPR experiments of supported and unsupported catalysts were carried out. $NiCo_2O_4$ and Co_3O_4 spinel oxides were prepared by thermal decomposition [1]. The supports used were TiO_2 (Anatase, Tioxide CLDD 1367, 19 m^2/g) and Grace SiO_2 (SP 2-324-382, 290 m^2/g). The $NiCo_2O_4$ catalyst was deposited on the supports by means of a standard pore-volume impregnation method: a known amount of an aqueous solution of $Ni(NO_3)_2 \cdot 6\ H_2O$ and $Co(NO_3)_2 \cdot 6\ H_2O$, mixed in stoichiometric amounts of 1 : 2, was added to the support. The samples were dried at a moderate temperature, and finally cured at T_F for 24 h to form the spinel oxide.

(V.2) Results and discussion

The TPR profiles of the unsupported $NiCo_2O_4$ (curve a) and Co_3O_4 (curves b and c) are shown in Fig. 5. Curve c is the TPR profile of commercial Co_3O_4 (Merck). The H_2/M values are given on the curves. The reduction profiles of $NiCo_2O_4$ and Co_3O_4 are similar. The reduction peaks are asymmetric and broad, indicating that various reducible species are present. It appears that the TPR of $NiCo_2O_4$ (curve a) takes place at lower temperatures than the reduction of Co_3O_4 (curve b) for both catalysts prepared under identical conditions.

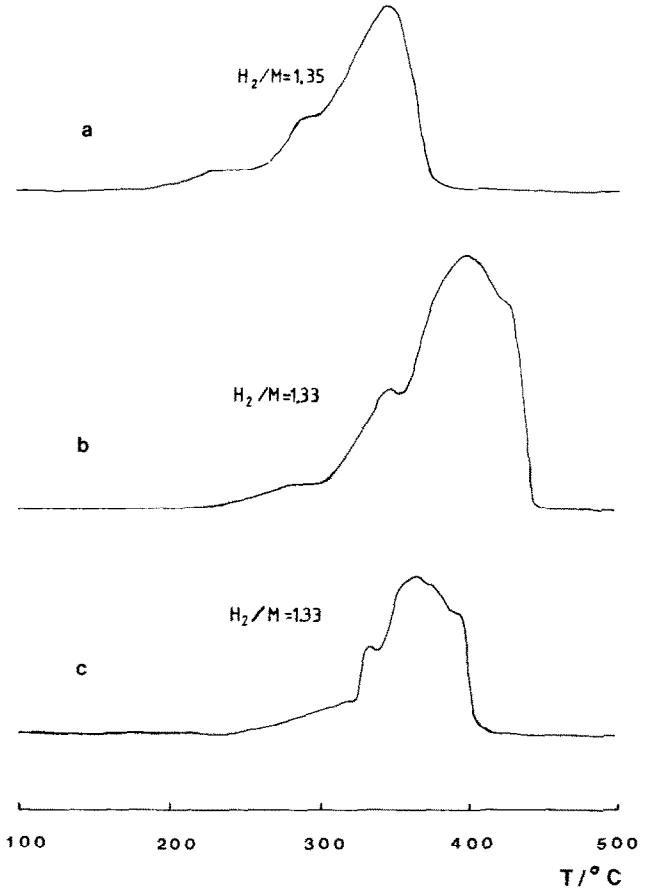

Fig. 5. TPR profiles of unsupported $NiCo_2O_4$ and Co_3O_4 catalysts. (a) $NiCo_2O_4$: 400°C for 1 h. (b) Co_3O_4: 400°C for 1 h; (c) Co_3O_4 (Merck).

This is most probably due to a difference in stability of the spinel oxides. It has been reported [10,19] that $NiCo_2O_4$ forms a "metastable" spinel structure, which breaks down already above 400°C, while Co_3O_3 is stable up to 900°C, as shown in the TGA curves in Section (II).

Two peak maxima are observed for both spinel oxides and suggest a two-stage process. Also the same stoichiometry is observed. The H_2/M value indicates that the average oxidation state of the metal cation before reduction is 2.67+. Table 4 gives a comparison of the TPR characteristic features of the literature data and this work. Paryjczak et al. [20] have performed a TPR study on Co_3O_4 prepared by coprecipitation and Martens [21] has studied Co_3O_4 supported on TiO_2. Our results are in agreement with the literature data.

TABLE 4

TPR characteristic features of Co_3O_4 and $NiCo_2O_4$

Sample	Peak maxima /°C		Peak area ratio	H_2/M	Ref
Co_3O_4 [a] ($T_F = 400$ °C; $t_F = 1$ h)	347	402	1:3	1.33	This work
Co_3O_4 (Merck) [a]	336	371	1:3	1.33	This work
Co_3O_4 (coprecip.) [a]	320	390	1·3	1.33	19
Co_3O_4/TiO_2 [b]	315	413	1:3	1.33	20
$NiCo_2O_4$ [a] ($T_F = 400$ °C; $t_F = 1$ h)	288	348	1:3	1.35	This work

[a] Unsupported.
[b] Supported.

The first step in the TPR of Co_3O_4, i.e. $Co^{2+}[Co^{3+}]_2O_4$, is the reduction of Co_3O_4 to CoO and the second step is the reduction of CoO to metallic Co, as follows:

$$Co_3O_4 + H_2 \rightarrow 3\ CoO + H_2O \qquad H_2/M = 0.33$$
$$3\ CoO + 3\ H_2 \rightarrow 3\ Co + 3\ H_2O \qquad H_2/M = 1.00$$
$$\overline{Co_3O_4 + 4\ H_2 \rightarrow 3\ Co + 4\ H_2O} \qquad \overline{H_2/M = 1.33}$$

From the observed peak ratio and the H_2/M ratio, a similar course of TPR of $NiCo_2O_4$ can be proposed:

$$NiCo_2O_4 + H_2 \rightarrow NiO + 2\ CoO + H_2O \qquad H_2/M = 0.33$$
$$NiO + 2\ CoO + 3\ H_2 \rightarrow Ni + 2\ Co + 3\ H_2O \qquad H_2/M = 1.00$$
$$\overline{NiCo_2O_4 + 4\ H_2 \rightarrow Ni + 2\ Co + 4\ H_2O} \qquad \overline{H_2/M = 1.33}$$

The reduction of the unsupported Co_3O_4 and $NiCo_2O_4$ takes place in two not clearly separated peaks. However, in the case of Co_3O_4 supported on TiO_2 [21], two clearly separated peaks were observed with H_2/M ratios of 0.33 vs. 1.00, which led to the two-step reduction model. Figure 6 presents the TPR profile of 7.15 wt% $NiCo_2O_4/TiO_2$ for different calcination temperatures T_F, i.e. 300 and 400 °C.

The two reduction peaks are now completely separated, and the start of the reduction, i.e. the first reduction maximum, takes place at temperatures lower than those in the case of the unsupported catalyst. This can be explained as a consequence of the particle size and distribution. It can be assumed from the properties of the supporting material that the $NiCo_2O_4$ particles of the supported catalyst are smaller and more uniform in size, whereas the unsupported particles are greater and have a less uniform particle size distribution. Similar particles have a relatively higher surface area, and thus relatively more surface defects where the reduction can start. The reduction of $NiCo_2O_4$ supported on SiO_2 also takes place in two separated peaks, and at temperatures lower than those for $NiCo_2O_4/TiO_2$. This is in accordance with the line of reasoning described above. The expected particle size on SiO_2 (290 $m^2\ g^{-1}$) will be smaller than that on TiO_2 (19 $m^2\ g^{-1}$). However, it was

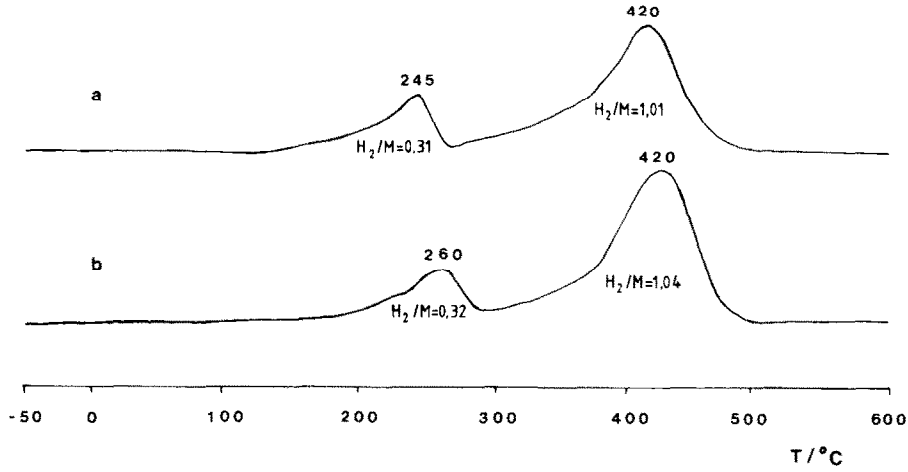

Fig. 6. TPR profiles of $NiCo_2O_4/TiO_2$ catalysts. (a) 7.15 wt% $NiCo_2O_4$: 300°C; (b) 7.15 wt% $NiCo_2O_4$: 400°C.

reported [20] that for Co_3O_4 supported on silica or alumina, the reduction takes place at higher temperatures. This was ascribed to an interaction between the active phase, the oxide and the support material. Our results indicate that there is no interaction between the $NiCo_2O_4$ catalyst, and SiO_2 or TiO_2. The compounds, i.e. nickel and cobalt titanates or silicates, responsible for the interaction are probably formed only at higher temperatures (T_F was 400°C maximum).

However, complete reduction of the supported $NiCo_2O_4$ takes place at higher temperatures than for the unsupported $NiCo_2O_4$ powders.

It can be assumed that the second stage in the reduction of the unsupported sample is faster because of the earlier presence of a metallic phase.

The total hydrogen consumption of the first vs. the second reduction peak is in the ratio of 1 to 3. The H_2/M value of 1.33 indicates that the stoichiometric oxide $NiCo_2O_4$ is formed and thus can be represented by the general formula $M^{2+}M_2^{3+}O_4$. If, instead of $NiCo_2O_4$, NiO and Co_3O_4 had formed on the support, the H_2/M value would have been 1.22, which is substantially different from the observed value. It is, however, not possible to determine the individual oxidation states of Ni and Co in $NiCo_2O_4$.

The ratios of the H_2/M values of both reduction peaks indicate a two-stage reduction. This mechanism assumes that no metallic phase is formed in the first reduction peak. This supposition was investigated in the next experiment. $NiCo_2O_4/TiO_2$ was reduced in a first TPR (Fig. 7, curve b) until the temperature of this first TPR was 280°C, which is the minimum in the hydrogen consumption between the two peaks (cf. Fig. 7, curve a). At this temperature, the reactor was flushed with argon and cooled down quickly to 25°C. The partly reduced oxide was then reduced in a second TPR run to 600°C (curve c). The reduction peak in the

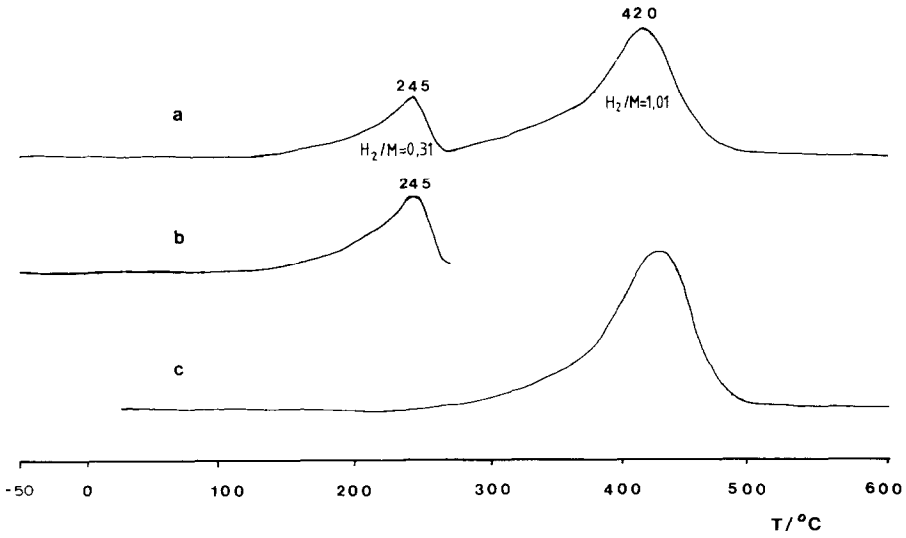

Fig. 7 TPR profiles of $NiCo_2O_4/TiO_2$ catalysts: 7.15 wt% $NiCo_2O_4$; 300°C. (a) TPR curve in the T range of −50 to 600°C; (b) first TPR curve in the T range of −50 to 280°C; (c) second TPR curve in the T range of 25 to 600°C.

second TPR coincides with the second peak of a TPR profile without interruption (curve a). It is known that in the presence of a metallic phase the reduction already starts at lower temperatures when the metallic phase is able to absorb hydrogen dissociatively. However, no shift of the second peak towards lower temperatures was observed. This experiment was also carried out for Co_3O_4 by Paryjczak et al. [20], who found that in the first TPR peak practically no metallic phase was formed (4% metal).

The influence of the temperature T_F, and the duration time t_F of the final heat treatment of $NiCo_2O_4$ on the TPR profile is shown in Fig. 8. A shift of the reduction peaks towards higher temperatures as a function of increasing T_F and t_F is observed.

For $T_F \geq 300°C$, the H_2/M ratio approaches the value of 1.33. The stoichiometric composition of $M^{2+}M_2^{3+}O_4$ is reached for $NiCo_2O_4$ with a mean cation valency of 2.67+. The increase of the H_2/M ratio at lower T_F is due to the increase in non-stoichiometry of $NiCo_2O_4$, as indicated by TGA in Section (II). Although the oxidation state of $NiCo_2O_4$ oxide is approximately the same above 300°C (T_F), the reducibility is different, as shown by the TPR profiles. The TPR curve appears to depend on the heat treatment. The reduction peaks are less separated at higher T_F and t_F. The changes in the TPR profiles are attributed to the changes in particle size and stability. The influence of the particle size was discussed above. The temperature at which the reduction starts increases with increasing T_F and t_F, and thus with decreasing surface area. This is corroborated by the BET surface area data, as

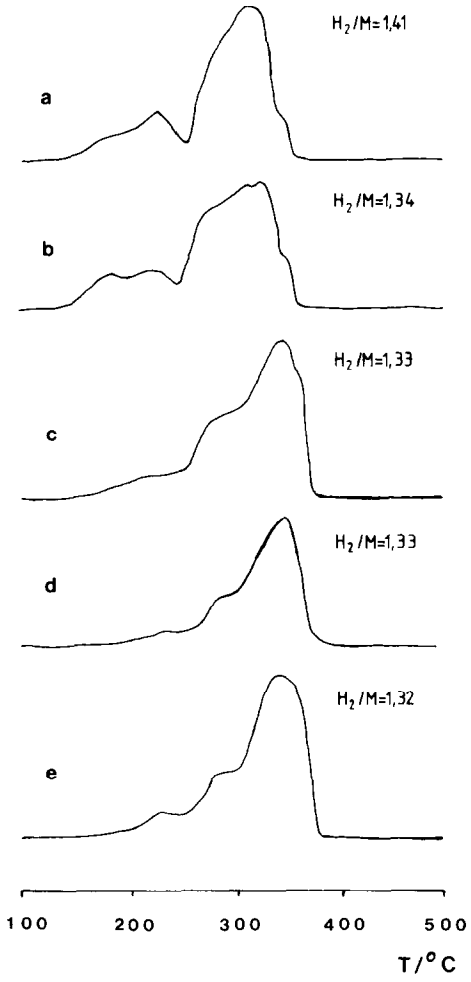

Fig. 8. TPR profiles of $NiCo_2O_4$ catalysts.

Curve	Heat treatment		BET surface area /$m^2\ g^{-1}$
	T_F/°C	t_F/h	
a	250	10	39.9
b	300	1	32.0
c	300	24	17.7
d	400	1	22.5
e	400	24	13.3

reported in Fig. 2. On the other hand, it can be assumed that the stability of the $NiCo_2O_4$ phase increases with T_F, resulting in a decrease in the reducibility.

So the reducibility of $NiCo_2O_4$ decreases with increasing T_F and t_F.

(VI) X-RAY AND AUGER PHOTOELECTRON SPECTROSCOPY

X-Ray photoelectron spectroscopy (XPS), also referred to as electron spectroscopy for chemical analysis (ESCA), and Auger electron spectroscopy (AES) were used to characterize and determine the composition of the surface of $NiCo_2O_4$ anodes as a function of the temperature of the final heat treatment (T_F). One of the major problems in the crystal chemistry of mixed oxide spinels is the determination of the valence state and the distribution of the cations among the octahedral and tetrahedral sublattices of the spinel structure, especially if two different metals are present, each of which can adopt more than one valence state. The binding energies and the satellite structure of the XPS photoelectron lines are indicative of the Ni and Co valence states in the charge distribution of $NiCo_2O_4$.

Auger electron and X-ray photoelectron spectra were recorded on a PHI 550 XPS/AES spectrometer equipped with a magnesium anode ($h\nu = 1253.6$ eV), an electron gun and a double-pass cylindrical mirror analyser. A PDP 11-04 computer interfaced with the spectrometer enabled signal handling to be carried out. The total pressure during the measurements in the spectrometer did not exceed 1×10^{-9} Torr. The XPS analyser was calibrated frequently and carefully with a gold sample (Au4$f_{7/2}$ at 83.8 eV). The C1s binding energy of contamination carbon was used for the internal calibration. No shift of the C1s line (284.6 eV) was observed, which indicates that no sample charging occurs. The reproducibility of the binding energy values was within 0.25 eV.

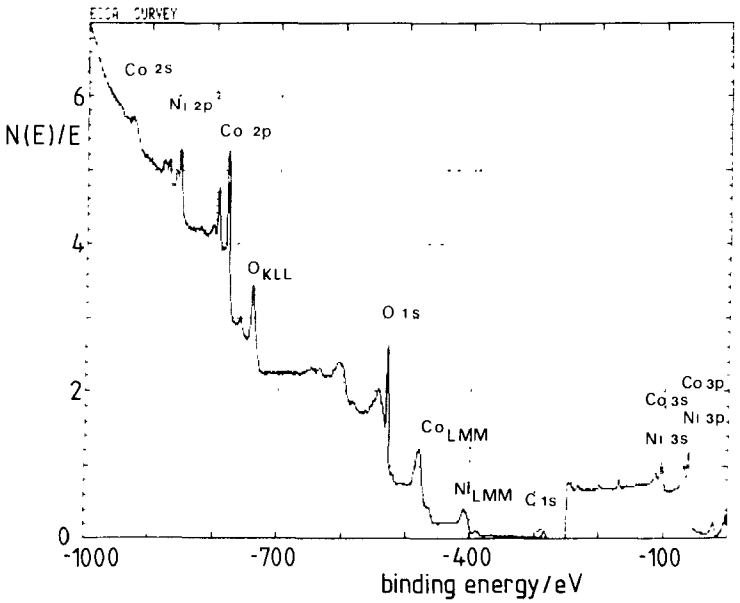

Fig. 9. XPS spectrum of a freshly prepared $NiCo_2O_4$ electrode. $T_F = 300\,^{\circ}C$ and $t_F = 1$ h.

The XPS survey scan for a freshly prepared $NiCo_2O_4$ electrode [1] is shown in Fig. 9. The survey scan is sufficient for the identification of all detectable elements present. Of course, predominantly the Ni2p, Co2p and O1s photoelectron lines are observed in this wide range spectrum. The carbon contamination C1s line is also observed.

The XPS concentrations of the various constituents were determined by measuring the peak area of the main photoelectron lines and by utilizing the atomic sensitivity factors, as presented by Wagner et al. [22]. This approach is satisfactory for quantitative work, except in the case of transition metal spectra with prominent shake-up lines. Therefore, the entire 2p region of nickel and cobalt, i.e. $2p_{3/2}$ and $2p_{1/2}$, was used when peak areas were measured. A generalized expression for the determination of the atom fraction of any constituent in a sample C_x, can be written as

$$C_x = \frac{n_x}{\sum_t n_t} = \frac{I_x/S_x}{\sum_t I_t/S_t} \tag{3}$$

where n is the number of atoms of the element per cm^3 of sample. I is the number of photoelectrons per second in a specific spectral peak and S is defined as the atomic sensitivity factor. The use of atomic sensitivity factors will normally furnish semiquantitative results (within 10–20%).

The surface compositions of $NiCo_2O_4$ electrodes, determined by XPS measurements as described above, are given in Table 5 for electrodes prepared freshly at temperatures T_F of 300 and 400°C, and for an electrode prepared at $T_F = 300$°C, which was aged by previously subjecting it to oxygen evolution. For freshly prepared $NiCo_2O_4$ electrodes, it appears that with lowering T_F, the Ni : Co ratio changes: the nickel concentration decreases while the cobalt content increases. Generally, it was found that the measured Ni : Co ratio (vs. nickel) for T_F equal to 400°C varied between the ratios 1.0 : 1.0 and 1.0 : 1.4, whereas for T_F equal to 300°C the ratio varied between 1.0 : 2.0 and 1.0 : 2.6.

The surface composition of the $NiCo_2O_4$ electrode changed after oxygen evolution at 0.5 A cm^{-2} for 24 h, as can be seen in Table 5: the nickel and cobalt concentrations decreased and the oxygen content increased. From this experiment it

TABLE 5

XPS compositions of $NiCo_2O_4$ electrodes

Materials	Elements/atom %			
	Ni	Co	O	C
$NiCo_2O_4$ (theor.)	14.3	28.6	57.1	—
$NiCo_2O_4$ 400°C for 1 h	21.4	22.1	48.1	8.4
$NiCo_2O_4$ 300°C for 1 h	12.3	32.1	47.0	8.6
$NiCo_2O_4$ 300°C for 1 h (after 24 h, 0.5 A cm^{-2})	8.8	28.0	52 2	11.0

is not clear whether the change is due to nickel or cobalt dissolution or whether it has to be attributed to an increase in oxygen species on the surface.

Summarizing, a considerable variation in the composition of the surface of freshly prepared $NiCo_2O_4$ electrodes was observed. Also, it was found that with increasing T_F, the surface composition deviates more from the theoretically expected one.

However, one must be aware that the experimental conditions of the XPS analysis can influence the quantitative results. Since XPS is a surface-sensitive method, which is performed under vacuum, in situ redox processes and hence surface decomposition of the $NiCo_2O_4$ sample can be induced by the X-ray radiation and the low partial oxygen pressure in the spectrometer, resulting in a change of the surface composition. On the one hand, surface enrichment or depletion of certain metal ions can take place, and on the other hand, a reduction of the sample would change the valence state of the metal ions. A study of the influence of the variation of the oxygen pressure in the spectrometer, and of the power of the X-ray source would give more evidence about these phenomena.

In view of the accuracy of the XPS analysis, it is not possible to make accurate quantitative analyses. Therefore, in the case of this study, the approach is useful for obtaining results in terms of orders of magnitudes. It can be concluded that lowering T_F tends to lead to Co enrichment and Ni depletion of the surface.

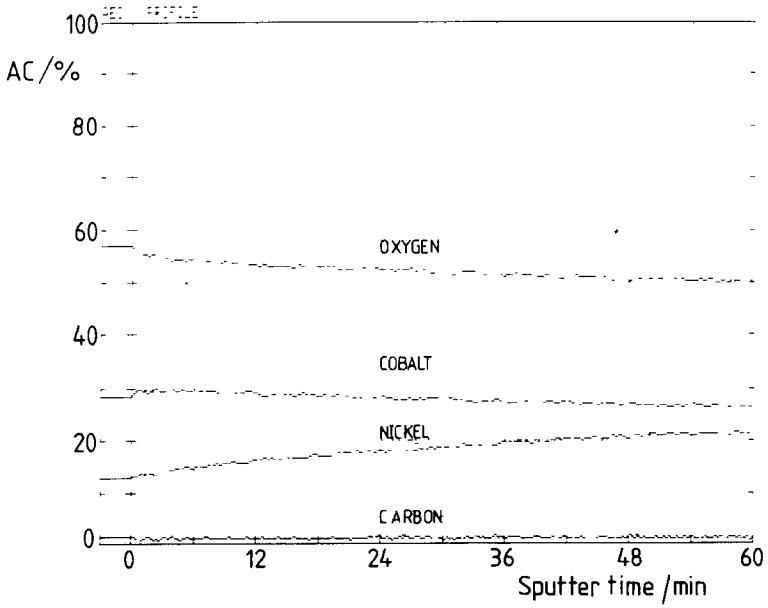

Fig. 10. Auger profile distribution of the elements in a fresh $NiCo_2O_4$ layer prepared at 300 °C (T_F) for 1 h (t_F).

Furthermore, it confirms that the surface composition is influenced by the temperature T_F, as indicated earlier by the voltammetric behaviour (see Part I) [2].

Auger spectroscopy was used to investigate the depth profile of the elements in

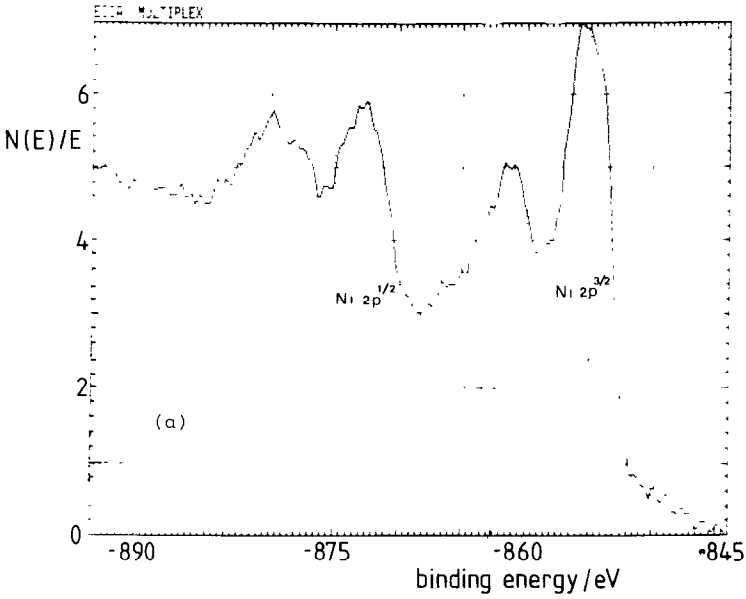

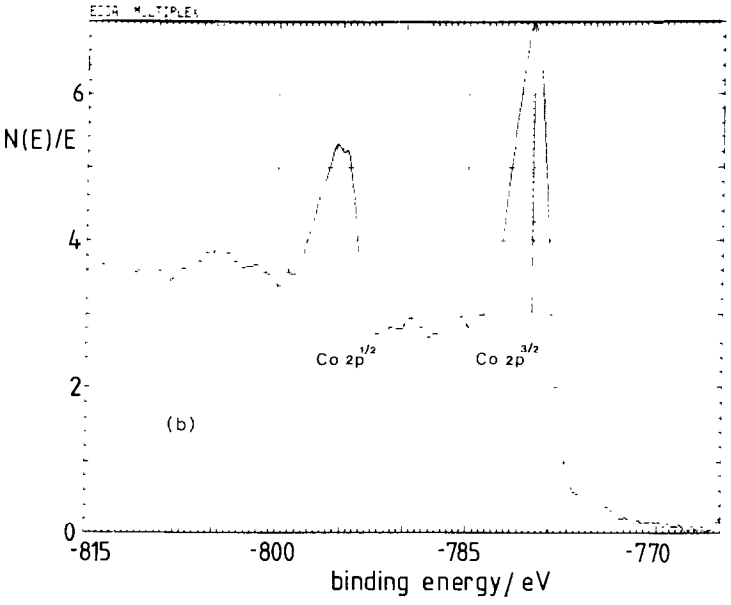

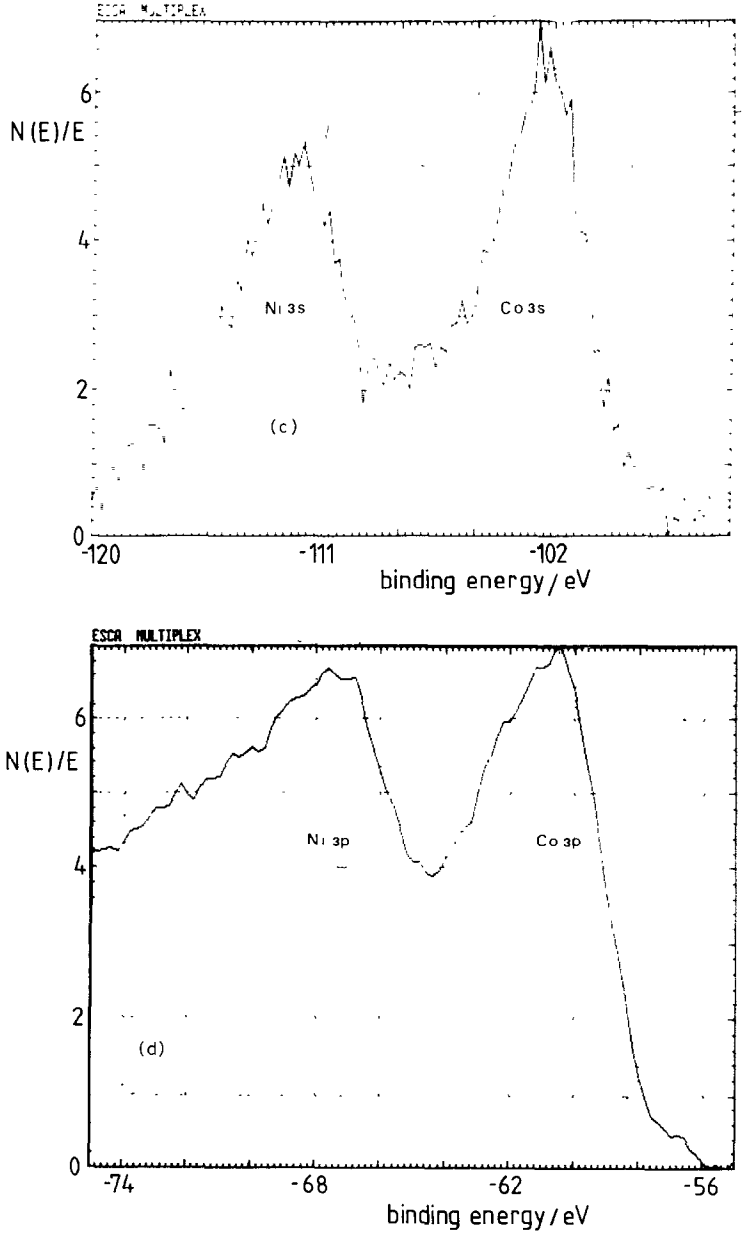

Fig. 11. Detailed scan of the XPS spectrum of a $NiCo_2O_4$ electrode. $T_F = 400\,^{\circ}C$ and $t_F = 1$ h. (a) Ni2p spectrum; (b) Co2p spectrum; (c) Ni3s and Co3s spectra; (d) Ni3p and Co3p spectra.

the $NiCo_2O_4$ layer. Depth profiling was accomplished by sputtering the surface with argon ions. The distribution of the elements as a function of depth into the specimen (sputtering time) is shown in Fig. 10 for $NiCo_2O_4$ prepared at $T_F = 300°C$. It appears that the nickel content increases with increasing sputtering time, whereas the cobalt and oxygen concentrations decrease slightly. However, one must remember that the experimental conditions can influence the AES analysis in a similar way, as mentioned earlier.

The detected carbon contamination in Fig. 10 is negligible compared to the values in Table 5. In the XPS experiments the detected carbon content varied significantly for $NiCo_2O_4$ electrodes prepared under similar conditions. Since the samples exhibit the carbon 1*s* peak in different quantities, we are inclined to believe that it is due to experimental conditions, i.e. C contamination in the spectrometer, and not due to the $NiCo_2O_4$ oxide sample preparation.

Some detailed spectra of the metal photoelectron lines are given in Fig. 11 and the binding energies (BE) for Co2$p_{3/2}$, Co3$p_{3/2}$, Co3*s*, Ni2*p*, Ni3$p_{3/2}$, Ni3*s* and O1*s* are given in Table 6. No influence of the temperature T_F, i.e. 300 vs. 400°C, on the spectral characteristics is observed. The Ni2*p* spectrum (curve a) of $NiCo_2O_4$ shows a prominent satellite structure and the Co2*p* spectrum (curve b) shows a weak satellite band. No satellite lines are observed in the Ni3*s* spectrum (curve c). The Ni3*p* spectrum (curve d), consisting of $3p_{3/2}$ and $3p_{1/2}$, shows an asymmetrical line with a weak satellite band. No satellite bands can be distinguished in the Co3*s* (curve c) and Co3*p* spectra (curve d); the adjacent Ni3*s* and Ni3*p* lines, respectively, can mask them.

XPS provides the ability to obtain information on chemical states from the variation in binding energy or chemical shifts of the photoelectron lines. Since the core levels of atoms may shift because of valence changes and different crystallographic sites, the splitting of core levels is direct proof of the presence of inequivalent atoms [23]. Unfortunately, it is not always possible to find separate peaks if the shifts are too small, as seen, for example, for the Co^{2+} and Co^{3+} states in Co_3O_4 [24]. In general, the binding energy of core levels shifts about 1 eV, through a change of the ionic charge of an atom by one unit, under the assumption that no other effects, such as covalency, are interfering. As the ligands are oxygen atoms for both lattice sites, covalency effects are supposed to have only a minor effect, and the

TABLE 6

Electron binding energies (in eV) for $NiCo_2O_4$

Ni2$p_{3/2}$	Δ [a]	Ni3$p_{3/2}$	Ni3*s*	O1*s*
855.2	17.35	67.5	111 8	529.3 530.7
Co2$p_{3/2}$	Δ [a]	Co3$p_{3/2}$	Co3*s*	C1*s*
779.85	15	60.75	102.6	284.6

[a] Δ is the difference in BE of the ($2p_{1/2} - 2p_{3/2}$) lines and gives the position of the $2p_{1/2}$ line.

TABLE 7

Core level energies (in eV) of nickel

	Ni^{2+} [23]	Ni^{3+} [23]	$NiCo_2O_4$
Ni2$p_{3/2}$	854.9	857.1	855.2
Ni2$p_{3/2}$ sat.	862.1	863 0	861.3

core levels M^{2+} and M^{3+} (M = Ni or Co) must be distinguishable. Comparison of Ni2$p_{3/2}$ of $NiCo_2O_4$ with those for Ni^{2+} or Ni^{3+} in other oxides [25], as given in Table 7, provides an indication that in $NiCo_2O_4$ nickel is present as a divalent ion. The Ni2$p_{3/2}$ and 3p spectrum shows a broadening of the lines as indicated by the full width at half minimum (FWHM) values given in Table 8, compared to that of other spinel oxides. This may be caused by the presence of another valence state. However, the formal oxidation state of cobalt appears to have little influence on the metal binding energies of Co compounds. The absence of any obvious relationship between the formal oxidation state of the Co metal and the metal binding energy has already been noted for Co oxides by McIntyre and Cook [27].

Figure 12 shows the O1s spectrum of a freshly prepared $NiCo_2O_4$ electrode and after oxygen evolution. The O1s spectrum for $NiCo_2O_4$ exhibits two peaks, one at 529.3 eV and a shoulder at about 530.7 eV.

Contradictory opinions have been reported as to the interpretation of the various O1s peaks which, for example, appear in the Ni–O [28–32] and Co–O [31–34] systems. It may be expected that not only lattice oxygen ions O^{2-}, but also chemisorbed species O_2, O_2^- and O^- oxygen in other chemisorbed molecules such as H_2O, CO, CO_2, etc., as well as surface and bulk hydroxides, could appear in the form of separate peaks.

The peak corresponding to the smaller binding energy, i.e. 529.3 eV, can be assigned to lattice oxygen ions O^{2-}. It was reported [27] that, in general, oxides of related metals which have identical crystallographic structures have very similar O1s binding energies. It appears that the lattice oxygen O1s binding energy of $NiCo_2O_4$ is about 0.6 eV lower with respect to that of the inverse spinel oxides $NiFe_2O_4$ and $CoFe_2O_4$ [27] and about 0.2 eV lower with respect to that of the normal spinel Co_3O_4 [32]. An empirical relationship between the O1s binding energy of the lattice oxygen and the valence state of the cation in oxides of the first transition metal

TABLE 8

Ni2$p_{3/2}$ and 3$p_{3/2}$ levels and FWHM for nickel spinels (in eV)

Compound	2$p_{3/2}$	FWHM	3$p_{3/2}$	FWHM of 3p	Ref
$Ni^{2+}_{0.1}Mn^{2+}_{0.9}[Ni^{2+}_{0.9}Mn^{3+}_{0.2}Mn^{4+}_{0.9}]O_4$	855.0	2.0	67 1	2.5	26
$Zn^{2+}[Ni^{2+}Mn^{4+}]O_4$	855.1	2.0	66.9	2.0	26
$NiCo_2O_4$	855.2	3.6	67.5	4.0	This work

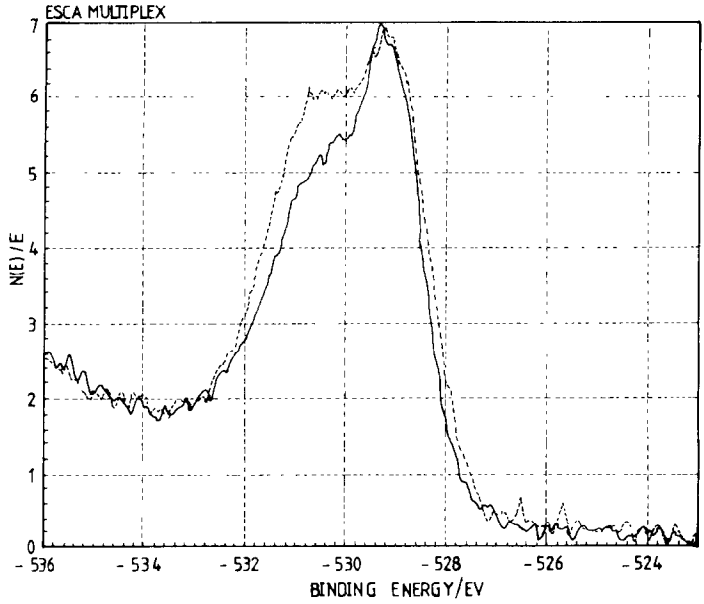

Fig. 12. O1s spectrum of $NiCo_2O_4$ prepared at $T_F = 300\,°C$ and $t_F = 1$ h. Freshly prepared $NiCo_2O_4$; (– – –) after oxygen evolution at 0.5 A cm^{-2} for 24 h in 5 M KOH.

series has been proposed by Haber et al. [32]. They reported that the O1s binding energy of Co_3O_4 indicated a mean valence state of the cations of 2.66+ . However, it does not predict the expected mean valence state 2.66+ when we apply it to other mixed inverse spinels such as $NiFe_2O_4$, $CoFe_2O_4$ and $NiCo_2O_4$. Thus, no simple relationship exists between the binding energy of the O1s photoelectron line and the chemical state.

The peak at higher binding energy is probably due to surface hydroxyl groups. Figure 12 shows the influence of oxygen evolution at a current density of 0.5 A cm^{-2} for 24 h in 5 M KOH on the O1s photoelectron line. An increase of the O1s peak at higher binding energy is observed, which indicates hydroxyl oxygen. Also, some potassium was detected on the surface by the appearance of the K2$p_{3/2}$ photoelectron line.

Sometimes evidence for certain valencies can be obtained from the presence of satellites, or multiplet splitting in the spectra.

In the Ni2p region of $NiCo_2O_4$ a prominent satellite band was observed, as shown in Fig. 11a, like that in NiO, $Ni(OH)_2$ and $NiFe_2O_4$ [27]. The satellite shoulder on the $2p_{3/2}$ line, as seen for NiO, does not occur. The prominent satellite structure in the Ni3s spectral region, which has been observed for NiO and $Ni(OH)_2$, is not seen for $NiCo_2O_4$, as for $NiFe_2O_4$ [27]. Only weak satellite lines are seen next to the $2p_{3/2}$ line in the Co2p spectrum.

The appearance of shake-up satellite lines near the M2p core lines (M = Ni or Co) was shown to depend on the paramagnetism or diamagnetism of the compound [35–37]. Frost et al. [35,36] have shown that high-spin Co^{2+} compounds have intense satellite bands associated with the 3s and 2p lines, while satellite lines for the low-spin Co^{3+} compounds are weak or missing.

The Co2p spectrum of $NiCo_2O_4$ shows an intermediate case. The intensity of the satellite structure indicates a mixture of Co^{2+} and mainly Co^{3+}.

Because of the absence of a strong shake-up satellite in the 2p spectrum, cobalt is mainly present as diamagnetic Co^{3+} ions in a low-spin state [38,39]. Furthermore, the Co2p spectrum reveals a weak shake-up satellite due to paramagnetic divalent high-spin cobalt. This is comparable with the mixed valence cobalt spinel oxide, i.e. $Co^{2+}[Co^{3+}]_2O_4$, which also shows only weak satellite lines in the Co2p spectrum [32]. Thus, it is possible to identify the presence of low-spin Co^{3+} and high-spin Co^{2+} on the basis of the satellite structure. The appearance of Co^{2+} may be caused by the reduction of Co^{3+} ions under the experimental conditions in the spectrometer.

(VII) CONCLUSIONS

From the TGA results, it can be suggested that non-stoichiometric $NiCo_2O_4$ spinel oxide is already formed at about 275°C, which is stable up to about 400°C, i.e. the stoichiometric composition. The weight loss above 400°C indicates the start of the breakdown of the $NiCo_2O_4$ spinel structure.

The BET experiments show the effect of the temperature T_F and duration time t_F of the final heat treatment on the surface area.

The X-ray data are in agreement with the TGA diagram and furthermore reveal that the decomposition of $NiCo_2O_4$ spinel oxide indeed sets in at temperatures above 400°C, with the appearance of NiO.

The TPR data indicate that the average oxidation state of the metal cation in $NiCo_2O_4$ before reduction is 2.67+ and that a stoichiometric oxide is formed which can be presented by the general formula $M^{2+}M_2^{3+}O_4$. Furthermore, at lower T_F an increase in non-stoichiometry of $NiCo_2O_4$ takes place, as indicated by TGA.

Summarizing, the $NiCo_2O_4$ XPS spectra can be distinguished from the individual nickel and cobalt oxides and they show some resemblance to those of similar mixed-valence spinel oxides, i.e. Co_3O_4, $CoFe_2O_4$ and $NiFe_2O_4$. Furthermore, the influence of the temperature T_F on the surface composition has been demonstrated.

The presence of divalent nickel has been proposed on the basis of the binding energy of the Ni2$p_{3/2}$ photoelectron line, and of Co as mainly diamagnetic Co^{3+} in a low-spin state and paramagnetic divalent high-spin cobalt, based on the satellite structure.

ACKNOWLEDGEMENTS

The authors are grateful to ir. J. Martens of the Eindhoven University of Technology (THE) for recording the TPR spectra and useful discussions, and to Dr. ir. V.A.M. Brabers (THE) for discussions on the interpretation of the XPS and Auger results. The BET experiments were carried out by the group of Professor J. Scholten at the Department of Chemical Technology, Delft University of Technology. The TPR experiments were carried out by the group of Professor R. Prins at the Department of Inorganic Chemistry, Eindhoven University of Technology.

REFERENCES

1 J. Haenen, W. Visscher and E. Barendrecht, J. Appl. Electrochem., 15 (1985) 23
2 J. Haenen, W. Visscher and E. Barendrecht, J. Electroanal. Chem., 208 (1986) 273.
3 C. Duval, Inorganic Thermogravimetric Analysis, Elsevier, Amsterdam, 1963.
4 D. Pope, D.S. Walker and R.L. Moss, J. Colloid Interface Sci., 60 (1977) 216.
5 R. Gararaglia, C.M. Mari and S. Trasatti, Surf. Tech. 19 (1983) 197.
6 V.V. Shalaginov, I.D. Belova, Yu.E. Roginskaya and D.M. Shub, Sov. Electrochem., 14 (1978) 1708.
7 D.L. Caldwell and M.J. Hazelrigg in M.O. Coulter (Ed.), Modern Chlor-alkali Technology, Ellis Horwood, Chichester, 1980, p. 221.
8 S. Angelov, E. Zhechera and D. Mehandjiev, Bulg. Acad. Sci., Commun. Dept. Chem., 13 (1980) 369.
9 O. Knop, K.I.G. Reid, Sutarno and Y. Nakagawa, Can. J. Chem., 46 (1968) 3463.
10 J. Robin and C. Bénard, C.R. Acad. Sci. Paris, 235 (1952) 1301.
11 W.J. King and A.C.C. Tseung, Electrochim. Acta, 19 (1974) 485.
12 M.R. Tarasevich, G.I. Zakharkin, A.M. Khutornoi, F.V. Markardei and V.I. Nikitin, J. Appl. Chem. USSR, 49 (1976) 1001.
13 D.H. Everett and R.H. Ottewill (Eds.), Proceedings of the International Symposium on Surface Area Determination, Bristol, 1969, Butterworth, London, 1970, p. 63.
14 W.F. McClune (Ed.), Powder Diffraction File of Inorganic Phases, International Centre for Diffraction Data, Swarthmore, PA, 1984.
15 M.R. Tarasevich and B.N Efremov in S. Trasatti (Ed.), Electrodes of Conductive Metallic Oxides, Part A, Elsevier, Amsterdam, 1980, p. 221.
16 F.K. Lotgering, Philips Res. Rep., 11 (1956) 337.
17 P.D. Battle and A.K Cheetham, Mat. Res. Bull., 14 (1979) 1013.
18 H. Boer, W.J. Boersma and N. Wagstaff, Rev. Sci. Instrum., 53 (1982) 349.
19 W.J. King and A.C.C. Tseung, Electrochim. Acta, 19 (1974) 492.
20 T. Paryjczak, J. Rynkowski and S Karski, J. Chromatogr., 188 (1980) 254.
21 J. Martens, H.F.J. van't Blik and R. Prins, J. Catal., 97 (1986) 200.
22 C.D. Wagner, W.M. Riggs, J.F. Moulder and G.E. Muilenberg, Handbook of X-Ray Photoelectron Spectroscopy, Perkin Elmer Corporation, Norwalk, CT, 1979.
23 M. Oku and K. Hirokawa, J. Solid State Chem., 30 (1979) 45
24 M. Oku and K. Hirokawa, J. Electron Spectrosc. Relat. Phenom., 8 (1976) 475.
25 K.T. Ng and D.M. Hercules, J. Phys. Chem . 80 (1976) 2094.
26 V A.M. Brabers, F.M. van Setten and P.S. Knapen, J. Solid State Chem., 49 (1983) 93.
27 N.S. McIntyre and M.G. Cook, Anal. Chem., 47 (1975) 2208.
28 K.S. Kim and N. Winograd, Surf. Sci., 43 (1974) 625.
29 K.S. Kim and R.E. Davis, J. Electron Spectrosc. Relat. Phenom., 1 (1972) 251.
30 C.R. Brundle and A.F. Carley, Chem. Phys. Lett., 31 (1975) 423.
31 W Dianis and J.E Lester, Surf. Sci., 43 (1974) 602.
32 J. Haber, J. Stoch and L. Ungier, J. Electron. Spectrosc. Relat. Phenom., 9 (1976) 459.

33 K. Hirokawa, F. Honda and M. Oku, J. Electron. Spectrosc. Relat. Phenom., 6 (1975) 333.
34 J.P. Bonnelle, J. Grimblot and A. D'Huyser, J. Electron. Spectrosc. Relat. Phenom., 7 (1975) 151.
35 D.C. Frost, C.A. McDowell and I.S. Woolsey, Chem. Phys. Lett., 17 (1972) 320.
36 D.C. Frost, C.A. McDowell and I.W. Woolsey, Mol. Phys., (1974) 27.
37 L. Yin, I. Adler, T. Tsang, L. Matienzo and S.O. Grim, Chem. Phys Lett., 24 (1974) 81.
38 B. Boucher, R. Buhl, R Di Bella and M. Perrin, J. Phys., 31 (1970) 113.
39 D. Scheerlinck and S. Houtecler, Phys. Status Solidi B, 73 (1976) 223.